J. Fluid Mech. (2001), *vol.* 432, *pp.* 285–311. Printed in the United Kingdom

Laboratory experiments on intrusive flows and internal waves in a pycnocline

By V. S. MADERICH[1], G. J. F. VAN HEIJST[2] AND A. BRANDT[3]

[1]Institute of Hydromechanics, Ukrainian Academy of Sciences, 8/4 Zheliabov Street, Kiev 252057, Ukraine

[2]Department of Physics, Eindhoven University of Technology, P.O. Box 513, 5600 MB Eindhoven, The Netherlands

[3]The Johns Hopkins University, Applied Physics Laboratory, Laurel, MD 20723, USA

(Received 28 June 1999 and in revised form 31 January 2000)

A laboratory study has been performed to simulate intrusive flows generated by internal wave-breaking activity in the oceanic pycnocline. Two different cases were considered. In the first set of experiments a short-duration source of motion was modelled by creating a finite region of well-mixed fluid. The collapse of this region resulted in intrusive flows and internal waves in the pycnocline. Attention was focused on the formation and subsequent evolution of solitary 'bulges' in the intrusion. Detailed flow measurements have revealed that the weak motion inside these bulges (which contain well-mixed fluid from the source) is organized in a four-vortex structure. Numerical flow simulations provided important information about the dynamics of this four-cell structure: the outer cells are associated with baroclinic generation of vorticity, while the inner cells are characterized by a balance between the advective and the viscous terms in the vorticity equation.

In the second set of experiments continuous mixing was induced by a vertically oscillating, horizontal grid centred in the pycnocline. The mixed region collapses, thus forming an intrusive flow into the pycnocline and internal waves that propagate along the pycnocline at higher speed than the intrusion. It was found that the velocity of the intrusive flow is approximately constant and that its dynamics is controlled by an inertial–buoyancy balance. The parameters of the internal waves in both cases were compared with theory.

1. Introduction

A well-known feature of stably stratified natural flows is the occurrence of intermittent, turbulent mixing events. Such local mixing events result in the creation of volumes of fluid with densities different from that of the ambient. Subsequently, buoyancy forces cause the lateral spreading of the mixed fluid along isopycnal surfaces, in the form of intrusive currents. In the ocean and the atmosphere, local turbulent mixing can be induced by a variety of mechanisms, for example by internal wave breaking, shear instability, convective overturning or by flow–topography interaction. Although these generation mechanisms may differ in scale and character, they commonly result in intrusive currents and possibly in internal waves in the stratified environment.

During the last three decades the problems of internal and boundary mixing have received considerable attention. Overviews of various aspects of these topics are

presented by Hopfinger (1987), Maderich, Nikishov & Stetsenko (1988), Fernando (1991), Garrett, MacCready & Rhines (1993) and Simpson (1997). Most experimental studies of mixed region collapse (starting with Wu 1969) and boundary mixing (see e.g. Browand & Hopfinger 1985; Ivey & Corcos 1982; Thorpe 1982; and more recently, Phillips, Shyu & Salmun 1986; Salmun & Phillips 1992; De Silva & Fernando 1998; Fonseka, Fernando & van Heijst 1998) were made for the case of linear stratification.

In natural situations, mixing events are often concentrated in a relatively thin pycnocline layer. This is nicely illustrated by observations in the Chesapeake Bay as described by Brandt *et al.* (1986*a*, *b*), where the frequent occurrence of high-frequency internal waves in the pycnoclinic region results from tidally driven shear across the pycnocline. In several instances the internal waves reached amplitudes of several metres (in a water column with a total depth of approximately 12 m), and subsequent breaking was observed. The variation of the internal wave activity was strongly correlated with the tidal phase, and the wave breaking was found to take place only at selected intervals. This breaking of internal waves resulted in intense vertical mixing within the stratified pycnocline, and hence in the occurrence of intrusive flow.

In the laboratory, the problem of collapse of a mixed fluid region within a pycnocline layer was first investigated by Amen & Maxworthy (1980), Maxworthy (1980) and Kao & Pao (1980). In particular, the effect of the pycnocline layer thickness on the intrusion and the internal waves resulting from the gravitational collapse were studied. For the case of a pycnocline thickness much smaller than the initial intrusion thickness, it was found that so-called solitary bulges were generated. These intrusive bulges consist of mixed fluid from the collapsed region. Similar bulges were observed in the experiments of Davis & Acrivos (1967) and Kamachi & Honji (1983), in which the mixed fluid region in the pycnocline was created by imposing a finite horizontal impulse. Recently, Stamp & Jacka (1995) have experimentally investigated the propagation of solitary internal waves of very large amplitude. In contrast to the predictions of small-amplitude theory and experiments, they found that the wavelengths increased with increasing wave amplitude. In their experiments, the wave forms were carefully created so as to generate only a single pulse wave form and to minimize the mode-1 tails and intrusions.

Although the cited studies have contributed to a better understanding of the various aspects of the dynamics of collapsing mixed regions, a few questions remain unanswered. The precise conditions required for the generation of solitary bulges, the details of the internal bulge structure and the interrelation between bulges and internal waves are not well understood. Another open question concerns the effect of the duration of the forcing (i.e. the mixing) on the intrusive flow.

The objective of the present experimental study is to compare investigations of intrusive flows in a pycnocline layer generated by instantaneous, event-like forcing (collapse of a mixed region) and by long-duration forcing (continuous stirring). In particular, the effect of the pycnocline thickness on the intrusion and internal waves will be investigated. In contrast to the study of Stamp & Jacka (1995) and other previous solitary wave experiments, the present study concerns relatively strong forcing (pulsed and continuous) that generates a combined solitary wave and intrusive flow field. Some preliminary results, focusing on internal wave propagation in the continuous stirring experiments, were presented by Brandt & van Heijst (1990), whereas Maderich & Kulik (1992) report on preliminary results obtained for the collapse experiments. The experimental arrangements and the measurement procedures are described in § 2. Results for the mixed-region collapse and grid-generated intrusion experiments are presented in §§ 3.1 and 3.2, respectively, and are compared with

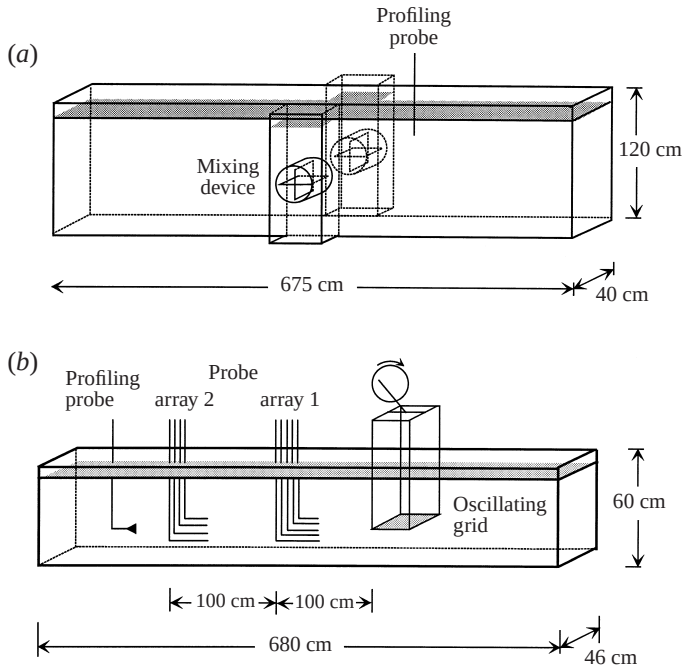

FIGURE 1. Schematic drawing of the experimental arrangements: (*a*) mixed-region collapse experiment, (*b*) oscillating-grid experiment.

results of numerical simulations and analytical predictions. Finally, the main results are summarized in § 4.

2. Experimental arrangements

2.1. *Experiments on the collapse of a two-dimensional mixed region in a pycnocline*

The experiments on a collapsing mixed region were conducted in a lucite tank 6.7 m long, 0.4 m wide and 1.2 m deep (see figure 1*a*) at the Institute of Hydromechanics in Kiev. The tank was filled with two homogeneous layers of salt water with densities ρ_1 and ρ_2 ($\rho_2 > \rho_1$). In order to obtain a sharp interface, water was siphoned off from the centre of the interface using two inverted funnels. A thicker interface was generated by local mixing induced by an oscillating wing, situated at one of the endwalls of the tank. Density profiles were measured by a vertically traversing conductivity probe that was developed by Levtsov & Chashechkin (1980).

A mixing device was situated in the centre of the tank, located at the centre of the pycnocline (interface). This device consisted of two horizontally aligned, thin-walled cylindrical tubes with internal diameters $2l_0 = 19.0$ cm, that are initially housed in two auxiliary tanks fixed to the sidewalls of the principal tank (see figure 1*a*). These tanks were filled with water to diminish the pressure difference between main and auxiliary tanks. The mixing tubes could be inserted from the auxiliary tanks into the main tank through circular slits in the sidewalls, thus isolating a cylindrical fluid volume from the ambient stratified fluid. The circular parts of the sidewalls, separating the fluid in the main tank from fluid in the auxiliary tanks, were each kept fixed by three thin supporting rods attached to the opposite wall of the auxiliary tank. The stratified fluid confined by the tubes was then mixed by two counter-rotating

four-lobe wire mixers. After the mixing was complete, the flexible-wire mixers were withdrawn through small circular holes, back into the auxiliary tanks, and the fluid in the mixing device was allowed to come to rest. By quickly withdrawing the tubes (through the circular slits) into the side tanks, the cylindrical mixed fluid region was released in the stratified ambient. In the subsequent stage, mixed fluid intrudes horizontally (in opposite directions) into the pycnocline. The flow was visualized by dye or by small tracer particles, and the evolution of the intrusive flow was recorded photographically. In order to obtain streak pictures of the flow relative to one of the advancing intrusions, a photo camera was mounted on a carriage system that was controlled to move at the same speed as the head of the intrusion.

To further investigate the internal structure of the flow in the intrusion head in detail, a limited set of additional experiments were carried out in a smaller tank, with dimensions 1.97 m long, 0.19 m wide and 0.3 m deep at the Fluid Dynamics Laboratory in Eindhoven. Again, the tank was filled with two homogeneous layers of different density, separated by a pycnocline. The total water depth measured 26 cm, and the centre of the pycnocline was situated 13 cm above the tank bottom. A mixed region was created either in a box located at one end of the tank, or on one side of a vertical barrier extending over the full depth of the water column. The mixing box, which spanned the width of the tank, was centred at the pycnocline and it had horizontal and vertical dimensions $l_0 = 6$ cm and $h_0 = 12$ cm, respectively. In the case of the full-depth barrier, the dimensions of the mixed region were $l_0 = 6$ cm and $h_0 = 26$ cm, respectively. Mixing of the fluid in the box was established by a two-lobe stirrer. After the mixing was completed and the mixed fluid had come to rest, the front wall (barrier) was quickly pulled upwards, and the mixed fluid subsequently intruded into the ambient stratified fluid. Flow visualization was carried out by using small tracer particles, which were illuminated by a vertical light sheet. The particle motions were recorded on video, and by use of a digital particle tracking system (DigImage) quantitative information about the associated flow field was obtained. For detailed information of the image analysis technique, see Dalziel (1993).

The two-dimensional velocity field (u, w) in the vertical plane (x, z), with x and z the lengthwise and vertical coordinates, obtained from the particle path data was interpolated onto a regular grid of 30×30 points by using cubic splines. The vorticity component normal to the vertical plane associated with this velocity field,

$$\omega = \frac{\partial w}{\partial x} - \frac{\partial u}{\partial z}, \tag{1}$$

was then calculated at each grid point. The corresponding stream function ψ was computed from the vorticity field by numerically solving the Poisson equation $\nabla^2 \psi = \omega$.

2.2. *Experiments on grid stirring in the pycnocline*

These experiments were conducted in a lucite tank 6.8 m long, 0.46 m wide and 0.6 m deep at the Applied Physics Laboratory of the Johns Hopkins University. This tank was filled with a stratified salt solution, so that the fluid consisted of a top layer and a bottom layer with uniform densities ρ_1 and ρ_2, and an intermediate pycnocline layer in which the density increased linearly with depth from ρ_1 to ρ_2. In all experiments the total depth of the fluid D measured approximately 48 cm. Turbulent mixing of the pycnocline fluid was induced locally by a vertically oscillating horizontal grid, positioned as shown in figure 1(*b*). This grid was constructed of 1 mm diameter wire woven into squares of dimensions $M = 0.63$ cm; the length, L_m, and width of the grid were 38 cm and 30 cm, respectively, while its thickness measured 2 mm.

The grid (in its mean position) was centred in the pycnocline. The induced stirring energy was controlled by the frequency of the grid oscillation, which had a fixed stroke of $S = 2.54$ cm. Most of the experiments were conducted at frequencies of $f = 2.0$ Hz, although a few additional tests were carried out with stirring frequencies of 1.6 Hz and 2.5 Hz. In the vicinity of the stirrer the mixed region collapses under gravity, thus forming an intrusive flow of mixed fluid into the pycnocline. The motion of this intrusion was visualized by introducing dye in the mixed fluid near the stirring grid. The speed of the advancing intrusion nose was calculated from photographs taken from the side of the tank at 5 s intervals in the area between 1 m and 2 m from the edge of the grid. In several experiments dye-producing crystals were dropped into the tank, and the subsequent distortion of their dye trails was recorded photographically. This information was used for calculating the vertical distribution of the longitudinal velocity above, below, inside, and ahead of the intrusion. Besides the intrusive flow, the collapse of the mixed region near the oscillating grid was observed to induce internal waves that propagated along the pycnocline at a higher speed than the intrusion. Two sets of micro-scale conductivity probes were used to measure the internal-wave activity. The probe rakes were positioned at 1.0 m and 2.0 m from the edge of the mixing grid, respectively, and each contained a vertical array of regularly spaced probes (see figure 1*b*). By use of these rakes, the vertical displacement of fluid associated with the travelling internal waves could be measured accurately.

Far downstream a temperature and conductivity profiling micro-scale probe was traversed vertically through the fluid to determine the temperature and salinity distribution in the stratified solution and thus the corresponding density values. This was done prior to and immediately after each experiment.

3. Results and analysis

3.1. *Mixed-region collapse*

3.1.1. *Experimental observations*

In general, the dynamics of the horizontal spreading of a symmetrical non-turbulent intrusion may be characterized by the thickness of the pycnocline, H, the total height of the water column, D, the thicknesses of upper and lower layers, D_1 and D_2 (these layer depths are measured with respect to the centre of the pycnocline, so that $D_1 + D_2 = D$), the density difference $\Delta\rho = \rho_2 - \rho_1$ across the pycnocline, the gravitational acceleration, g, the initial vertical and horizontal dimensions of the intrusion, h_0 and l_0, and the kinematic viscosity ν.

The density distribution can be closely fitted by a hyperbolic-tangent profile

$$\rho(z - z_0) = \rho_0[1 - (\Delta\rho/2\rho_0)\tanh(\alpha(z - z_0))], \tag{2}$$

where $z = z_0$ is the level of the pycnocline centre and $\rho_0 = (\rho_1 + \rho_2)/2$. The pycnocline thickness is defined as $H = 2\alpha^{-1}$. Typical examples of stratification profiles from the mixed-region collapse experiments are given in figure 2. The values of the experimental parameters are presented in table 1. Series 1, 2 and 3 concern experiments carried out in the large tank, whereas the small-tank experiments are listed as series 4. As can be seen from this table, in the various runs the parameters $\Delta\rho$, D and H (and thus α) were changed systematically.

The evolution of the symmetric intrusion can be defined as a function of time t by

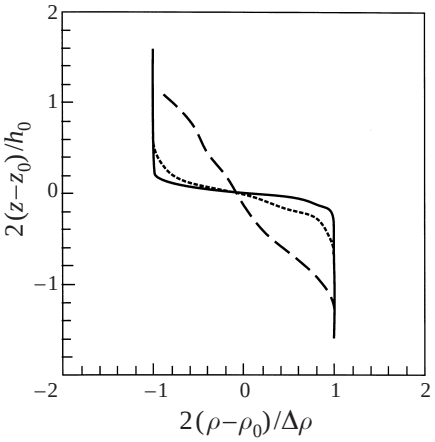

FIGURE 2. Normalized density profiles measured in the mixed-region collapse experiments 101 (——), 102 (– - –) and 103 (- - -); for experimental parameter values, see table 1.

Exp.	$\Delta\rho$ (g cm^{-3})	D (cm)	h_0 (cm)	α^{-1} (cm)	a (cm)	U_i (cm s^{-1})	U_w (cm s^{-1})	θ	ϕ	Re_0
101	0.0038	76	19	1.2	2.8	1.98	—	0.25	7.92	4349
102	0.0038	76	19	2.4	2.5	2.11	—	0.25	3.96	4349
103	0.0038	76	19	13.6	1.4	—	3.50	0.25	0.70	4349
105	0.0042	76	19	1.1	2.5	2.01	—	0.25	8.04	4572
106	0.0042	76	19	6.1	2.2	—	2.80	0.25	1.56	4572
107	0.0042	76	19	8.5	1.5	—	3.20	0.25	1.12	4572
201	0.0067	76	19	1.2	2.4	2.70	—	0.25	7.92	5775
202	0.0080	76	19	1.1	2.3	2.91	—	0.25	8.04	6310
203	0.0162	76	19	1.1	2.2	3.92	—	0.25	8.04	8924
301	0.0048	38	19	1.2	2.8	2.06	—	0.5	7.92	4785
302	0.0046	19	19	1.2	2.6	1.91	—	1.0	7.92	4888
303	0.0046	19	19	5.3	—	—	—	1.0	1.80	4785
401	0.0071	26	12	1.0	2.3	2.10	—	0.46	6.0	2715
402	0.0071	26	26	1.0	2.9	2.30	—	1.0	13.0	8660
403	0.0091	26	12	1.0	1.8	2.23	—	0.46	6.0	3074

TABLE 1. Mixed-region collapse experiments.

the non-dimensional function

$$l(t)/l_0 = f_l(N_s t, Re_0, \phi, \theta, \delta). \tag{3}$$

Here $l(t)$ is the half-length of the symmetrical intrusion, l_0 is the initial half-length of the intrusion, $Re_0 = h_0^2 N_s/4\nu$ is the initial Reynolds number of the intrusion, $N_s = (g\Delta\rho/h_0\rho_0)^{1/2}$, $\delta = 2l_0/h_0$, $\phi = h_0/H$ and $\theta = h_0/D$.

Wu (1969) recognized the three subsequent stages of collapse (initial, principal and viscous), which were described by the following power-law dependences

$$(l(t) - l_0)/l_0 = (Nt)^{m_1},\ l(t)/l_0 = (Nt)^{m_2},\ l(t)/l_0 = (Nt)^{m_3}, \tag{4}$$

Author	Comments	θ	ϕ	m_1	m_2	m_3
Kao (1976)	Theoretical value	$\ll 1$	$\ll 1$	2	1/2	—
Padmanabhan et al. (1970)	Theoretical value	$\ll 1$	$\ll 1$	—	—	1/6
Wu (1969)	Mean experimental value	0.25	0.25	1.08	0.55	—
Amen and Maxworthy (1980)	Mean value for runs with $\delta = 1$	0.76	0.76	—	0.75	—
Maxworthy (1980)	Experiment	0.14	2	—	0.85	—
Abramian and Kudin (1983)	Mean experimental value	0.1	0.1	—	—	0.17
This study	Exp. 103	0.25	0.70	—	?	0.14
	Exp. 106	0.25	1.56	—	0.65	0.12
	Exp. 102	0.25	3.96	—	0.93	—
	Exp. 105	0.25	8.04	—	0.95	—
	Exp. 303	1.0	1.80	—	0.87	0.12
	Exp. 302	1.0	7.92	—	0.94	—

TABLE 2. Numerical values of the exponents m_1, m_2, m_3 for the three stages of the intrusion collapse.

respectively. The numerical values of the exponents m_1, m_2 and m_3 in the power-law relations (4) for the three stages of the intrusion collapse in the two-dimensional case are given in table 2. For a deep linearly stratified ambient fluid layer theoretical estimates for initial and principal stages were obtained by Kao (1976), whereas Padmanabhan *et al.* (1970) obtained a self-similar solution for the final stage. The experimental values for the principal and final stages for an intrusion collapsing in a deep layer (see Wu 1969; Abramian & Kudin 1983) are in good agreement with the theoretical estimates, in contrast to $m_1 \approx 1$ (Wu 1969) which is not in agreement with the theoretical value $m_1 = 2$ (Kao 1976). Amen & Maxworthy (1980) showed that internal wave generation has to be taken into account in order to obtain a better fit to the experimental data in the initial stage. Considerable departures of m_2 from the theoretical value 1/2 were found in the experiments of Amen & Maxworthy in a 'shallow' linearly stratified tank ($\phi > 0.5$). The formation of internal solitary waves from the collapse of a mixing region in a thin pycnocline ($\phi > 1$) was observed by Maxworthy (1980) and Kao & Pao (1980). These waves propagate with gradually decreasing speed. Although previous studies have provided substantial information about the formation of waves during the collapse, the evolution and the internal structure of the intrusion appear to have received much less attention.

To gain a better insight into the formation mechanism and the subsequent evolution of solitary 'bulges' in the intrusion we have performed four series of experiments (see table 1). In the first and second series we investigated the dependence of the collapse on the parameters ϕ and Re_0, while the other parameters were kept fixed ($\theta = 0.25, \delta = 1$). The influence of the total tank depth (D) and the pycnocline thickness (H) on the intrusion dynamics was studied in the third series of experiments. The fourth series was carried out with the aim to study the internal structure of the bulges.

At moderate ϕ-values the collapse evolves as in the case of a linear stratification (Amen & Maxworthy 1980). The sequence of photographs in figure 3(a) shows the evolution of the collapse process for the particular case $\phi = 1.56$ (exp. 106). Just after the mixed region is released, the collapse induces a large-amplitude wave in the pycnocline. Initially, the head of the intrusion was more or less coupled with this propagating wave, so the spreading velocity of the intrusion was very close to the wave velocity. After some time, however, the wave moved ahead of the intrusion nose and travelled forward as a single wave, like in the experiment of Maxworthy (1980).

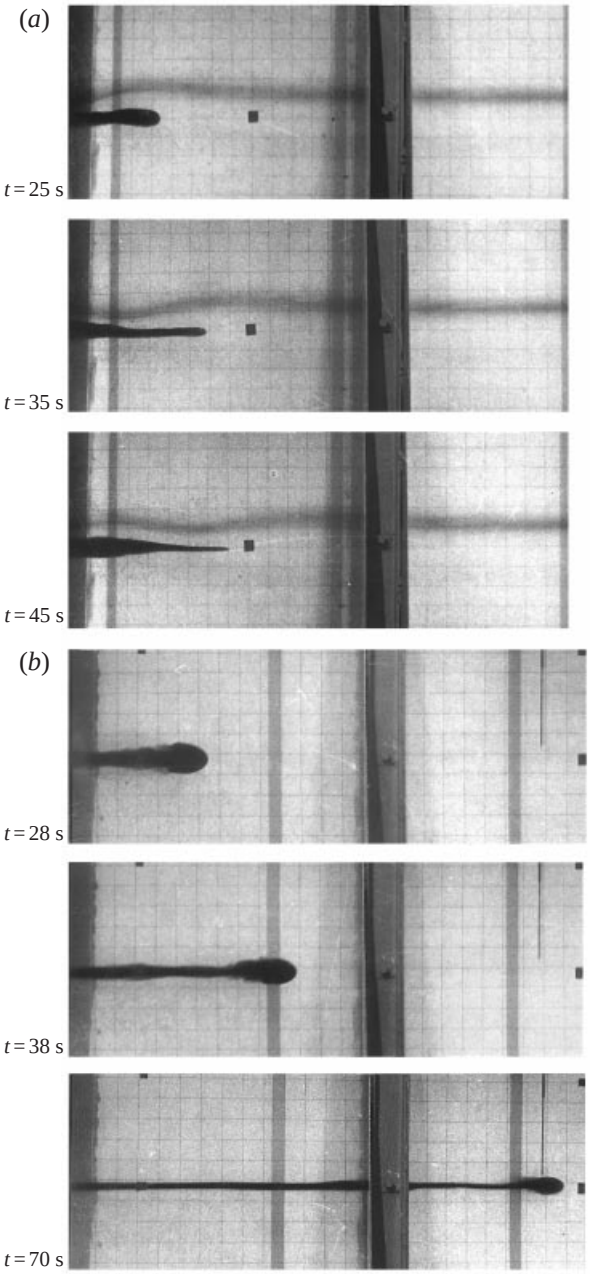

FIGURE 3. Sequences of photographs illustrating the evolution of the dye-visualized intrusion in two different experiments: (*a*) $\phi = 1.56$ (exp. 106), for $t = 25$ s, 35 s, 45 s; (*b*) $\phi = 8$ (exp. 105), for $t = 28$ s, 38 s, 70 s. In both experiments the density difference was $\Delta\rho = 0.0042\,\mathrm{g\,cm^{-3}}$. The grid at the back wall consists of 5 cm squares, while the little black squares are markers fixed at the front wall; their horizontal separation distance is 1 m. Unfortunately, the view is partially hindered by the metal bar (vertical dark band), which is part of the tank frame. In (*a*) a horizontal layer of dye was added prior to the start of the experiment; the distortions of this dye layer clearly indicate internal wave motion.

At this stage the propagating intrusion nose slowed down, and in some cases even a weak retrogade motion of the head was observed. Subsequently, the nose was again pushed forward over a small distance when new waves of smaller amplitudes passed by. In the final stage the intrusion acquired a sharp-nosed shape, indicative of the viscous regime.

The evolution of the intrusion has a qualitatively different character when the pycnocline thickness H is much smaller than the initial intrusion thickness h_0 (i.e. $\phi \gg 1$), as illustrated by the sequence of photographs shown in figure 3(*b*) for the case $\phi = 8$ (exp. 105). Observations revealed that wave radiation ahead of the intrusion was, in this case, absent. The dye visualization provided clear evidence of flow instability behind the intrusion head during the initial stage of evolution (figure 3*b*, frames 1, 2). However, this turbulent motion was observed to decay quickly, after which the intrusion acquired an elliptical shape: the frontal bulge propagated with an almost constant speed horizontally through the ambient stratified fluid (figure 3*b*, frame 3).

Careful inspection of the dye-visualization photographs revealed the occurrence of one or two additional smaller bulges in the intrusion. The existence of these secondary bulges was also confirmed by conductivity probe measurements, which revealed a coupling between the intrusion bulges and symmetric internal waves in the ambient stratified fluid. The bulges in figure 3*b* and in Maxworthy's (1980) figure 5 are similar in appearance. A quantitative analysis of the bulges is given below.

3.1.2. *Numerical simulations*

In order to further explore the detailed nature of the evolving intrusion and internal wave a numerical simulation of the laboratory experiments was performed. The unsteady flow was assumed to be laminar, two-dimensional and governed by the Navier–Stokes equation in the Boussinesq approximation. The problem was solved by using finite differences, with a splitting scheme similar to that described by Guschin (1981). The corresponding pressure field was obtained by a modified MAC method. In view of the experimental configuration, the evolving intrusive flow was assumed to be symmetric with respect to the vertical plane through the initially cylindrical volume of intruding fluid, so that only one half of the flow domain needed to be considered. This computational x, z-domain was covered by a 128×128 grid. No-slip conditions were prescribed on the boundaries, except for the mid-plane boundary, where symmetry conditions were applied.

Figure 4(*a*) shows results of the numerical simulation for times corresponding to those of the experiment (figure 3*a*). The plots show the non-dimensional density deviation $\delta\rho = (\rho - \rho_0)/\Delta\rho$ and the spatial distribution of passive markers that were put in the initial cylindrical region of mixed fluid prior to the collapse. In general, the calculated intrusion agrees well with the observations, with respect to its shape, its advance speed and the internal solitary wave formation. The results of the numerical simulation of the marker distributions for the case $\phi = 8$ (the experiment shown in figure 3*b*) are presented in figure 4(*b*). As in the previous case, the calculations agree quite well with the observed evolution of the dyed intrusion. Careful inspection, however, reveals that the calculated propagation speed is approximately 10–15% larger than the measured nose velocity. Also, in the simulated flow the instability just behind the bulge is much weaker than in the experiment. These discrepancies are most likely due to viscous effects near the sidewalls and to the coarseness of the calculation grid.

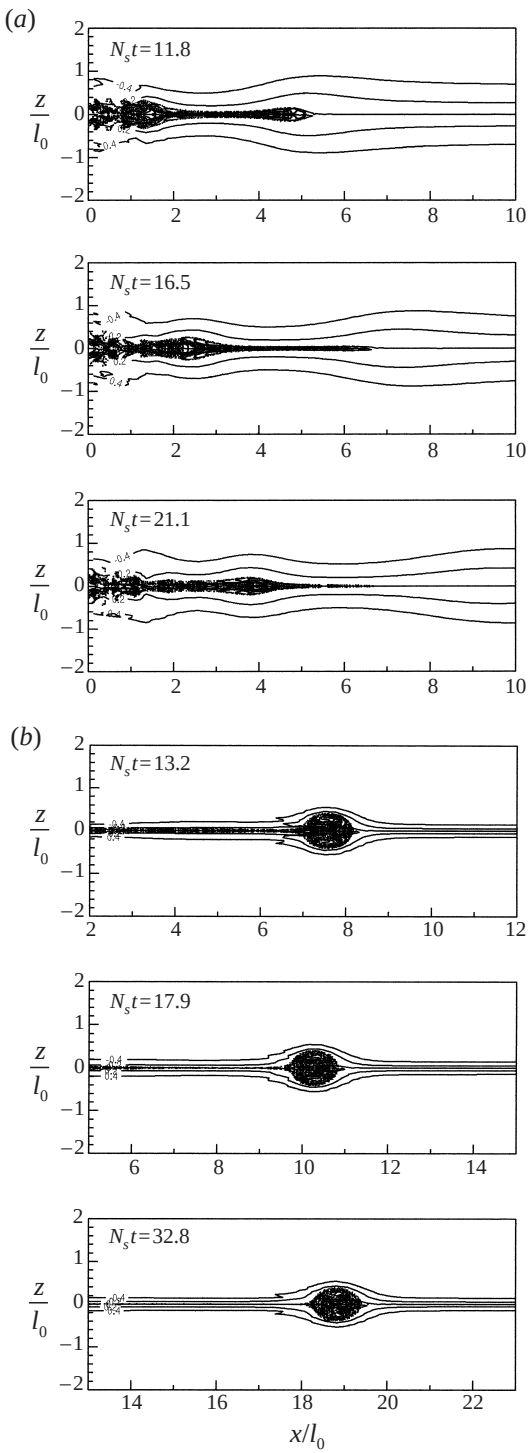

FIGURE 4. Sequences of plots showing the computed evolution of the intrusion (visualized by markers) according to the initial states of (*a*) exp. 106, and (*b*) exp. 105. The plots are drawn for times corresponding with those of the photographs in figure 3.

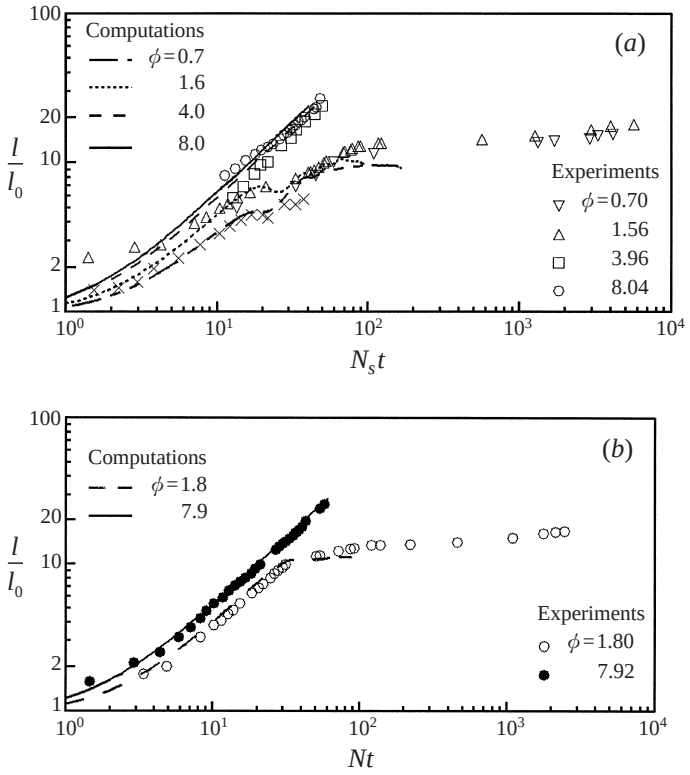

FIGURE 5. Measured normalized intrusion length l/l_0 as a function of the scaled time $N_s t$ in the experiments (*a*) 102, 103, 105, 106 and (*b*) 302, 303. The curves represent the results of the numerical simulations of the present experiments. Data of Amen & Maxworthy's (1980) experiment 105 are indicated by crosses.

3.1.3. *Experimental results*

For experiments of series 1–3, the advance of the intrusion nose was measured from photographic recordings of the dye-visualized intrusion. The results for series 1, spanning the range $0.7 < \phi < 8$, with $Re_0 \approx 4500$, are presented in figure 5(*a*). The distinction between the $\phi \lesssim 1$ cases (thick pycnocline: rapid slow-down of the intrusion) and the $\phi \gg 1$ cases (thin pycnocline: propagation at approximately constant speed) is easily observed. Two stages are clearly visible for experiments 103 and 106, namely the principal and final stages. The exponent m_2 for exp. 105 ($\phi = 1.56$) is 0.65, which is less than in the corresponding experiments of Amen & Maxworthy (1980); the data of their experiment 105 (for $\delta = 1, \phi = \theta = 0.72$, with a value $m_1 = 0.71$) are presented in figure 5(*a*) by the crosses. There is a small difference between the evolution of the intrusion in the viscous stage in experiments 103 and 106 with the value $m_3 \approx 1/6$, suggesting a weak dependence on the initial stages of the intrusion process. Figure 5(*b*) shows data of two experiments of series 3 (exps. 302 and 303) with the same $\theta = 1$ but different ϕ-values ($\phi = 7.92$ and 1.8, respectively). Qualitatively, these plots are the same as those in figure 5(*a*) (exps. 105 and 106), so it appears that ϕ is the main parameter that governs the intrusion dynamics. The exponent $m_2 = 0.87$ for exp. 303 is somewhat larger than the value found in experiments 103 and 106.

The values of $l(t)/l_0$ as obtained from the numerical simulations are also plotted in figure 5(*a*) for the same ϕ-values. The calculations show good agreement with

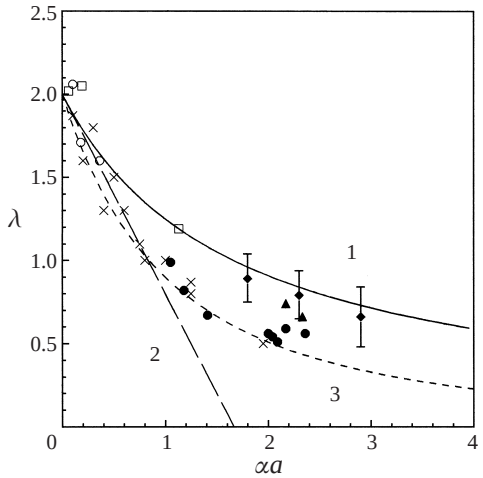

FIGURE 6. Experimental data for the wave speed parameter λ as a function of the non-dimensional amplitude αa. The symbols represent: ○, series 1 and 2; △, series 3; and ◇, series 4 of the collapse experiments; □, oscillating grid experiment; ×, Davis & Acrivos (1967). The filled symbols represent cases in which bulge formation was observed. The curves labelled 1, 2 and 3 represent the theoretical predictions (5) and (7), and the numerical results (8) of Terez & Knio (1998), respectively, as discussed in the text.

the experimental data for $N_s t < 100$. It should be noted that the use of the explicit numerical scheme is limited, and that it is less suited for modelling the slow viscous collapse process in very thin intrusions.

The advance speed, U, has been compared with the displacement amplitude, a, of the isopycnals induced by the intrusion. The amplitude a was determined as the half-thickness of the frontal bulge or as the maximum vertical displacement of a dye layer near the intrusion. The results are presented in figure 6, in which the non-dimensional wave speed parameter $\lambda = g \ln(\rho_1/\rho_2)/2\alpha U^2$ introduced by Davis & Acrivos (1967) is plotted versus αa, with $\alpha = 2/H$ the inverse pycnocline half-thickness, as defined above.

In the approximation of weakly nonlinear long internal waves in a pycnocline between two deep homogeneous fluid layers one may apply the Benjamin–Ono equation, which has algebraic soliton solutions. The curve labelled 1 in figure 6 corresponds to the formula for weakly nonlinear internal waves in the Boussinesq approximation:

$$\lambda = 2.0/(1 + \tfrac{3}{5}\alpha a), \tag{5}$$

with the wave velocity U_w defined according to Benjamin (1967):

$$U_w = \left\{ \frac{g\Delta\rho}{4\alpha\rho_0}(1 + \tfrac{3}{5}\alpha a) \right\}^{1/2}. \tag{6}$$

The broken line labelled 2 in figure 6 represents the Davis & Acrivos (1967) formula

$$\lambda = 2.0 - 1.2\alpha a. \tag{7}$$

In the weakly nonlinear approximation the propagation speeds observed in the collapse experiments are correctly described by (7) for $\alpha a \lesssim 0.3$, as one would expect on the basis of the small-parameter expansion in this theory. As one observes, relation (7) even fits the experimental data up to values $\alpha a \lesssim 0.8$. For $\alpha a > 1$ serious

discrepancies occur. The Benjamin formula underestimates the measured propagation speeds, while on the other hand, the Davis–Acrivos relation (7) overestimates the intrusion velocity for $\alpha a > 1$. Additional experiments in which the water depth was changed systematically (series 3, see table 1), revealed that the advance speed U decreases with decreasing depth, as can be observed from the increased λ-values, see figure 6. The results of measurements on waves generated by the impulsive motion of a plunger (Davis & Acrivos 1967) are also plotted in figure 6 (indicated by the crosses). It turns out that the relation between λ and αa for waves generated by the intrusion collapse closely matches that of waves originating from an impulse source.

The curve labelled 3 corresponds with

$$\lambda = 2.0/(1 + 0.49\alpha a)^2, \tag{8}$$

which represents the fit to the numerical results of Terez & Knio (1998). As one can clearly see, the experimental data lie in a band between curves 1 and 3. Apparently, relation (8) provides a lower boundary for the measured λ-values.

3.1.4. *Experimental and numerical study of the bulge structure*

As remarked before, for small pycnocline thicknesses ($\phi \gg 1$) the intrusion head took on the appearance of an elliptical bulge. As apparent from figure 5, the propagation speed is close to constant in time, showing only a weak, gradual decrease. Analysis of the experimental data has revealed that the Froude number of the bulge, defined as $Fr = U/(2ag\Delta\rho/\rho_0)^{1/2}$, is approximately constant. The mean Fr-values measured in the deep-tank experiments (series 1 and 2; $\theta = 0.25$) and shallow-tank experiments (series 3 and 4; $\theta \geqslant 0.5$) were 0.48 and 0.37, respectively. The role of viscosity was relatively weak: the bulge Reynolds number $Re = 2aU/\nu$ was varied in the range 600–1200.

An important question concerns the internal structure of the intrusion bulge. This question is more generally stated as: what is primary in the bulge dynamics – internal wave or intrusional motion? Maxworthy (1980) assumed that the mixed fluid in the intrusion head is trapped within the leading solitary wave. In that case the dynamics of collapse-generated bulges should be similar to that of bulges of intrusions generated by application of some source of impulse (Davis & Acrivos 1967; Hurdis & Pao 1975; Kamachi & Honji 1982; Flór, Fernando & van Heijst 1994). Kamachi and Honji have taken streak photographs with a camera moving with the bulge, which revealed that two sets of nested closed streamlines occur in the bulge for amplitudes $\alpha a \geqslant 1.2$; this is referred to as the 'vortex-pair type' bulge. In contrast, for $\alpha a < 1.2$ the bulge is of the 'internal-wave type', in which the streamlines (in the co-moving frame) are all open. A theoretical model of the vortex-pair type bulge was recently proposed by Chernyshenko (1993) for the case of large Reynolds numbers. In this model it was assumed that both the vorticity and the density within the cells formed by the closed streamlines are uniform.

In another approach, Kozlov & Makarov (1990) assumed that the fluid in the mixed bulge is at relative rest, i.e. moves through the pycnocline as a solid body with zero vorticity. This type of bulge was named 'solidon' (contraction of the words soliton and solid body). By assuming that these inviscid bulges acquired a stationary shape and a constant propagation speed, Kozlov & Makarov were able to construct an approximate analytical solution for the solidon. They found that the integral characteristics of this solidon solution (shape and propagation speed) are in close agreement with experimental data. The same authors performed a numerical simulation of this solidon bulge by the method of contour dynamics, and they found

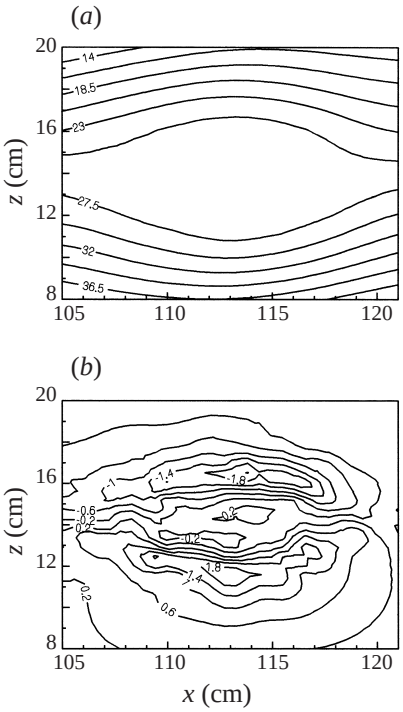

FIGURE 7. Plots of (*a*) the streamline pattern in a co-moving frame and (*b*) the vorticity distribution in the bulge as measured in experiment 401 (table 1) at $t = 56$ s.

that the solidon is unstable in the sense that Kelvin–Helmholtz billows developed. Subsequently, the rear part of the bulge transformed into a smaller, more slowly travelling bulge, and the instability was seen to start again. In the experimental situation, however, this type of instability is only observed in the initial stage of the bulge formation, not during its subsequent evolution (see figure 3*b*).

To resolve these discrepancies the internal structure of the bulge was investigated in more detail. Streak photography by a co-moving camera revealed that in the mixed-region collapse experiments the motion inside the bulge is very weak. Apparently, it is neither of the large-amplitude internal-wave type nor of the vortex-pair type, in contrast to the observations by Kamachi & Honji (1982) and others. Obviously, the way in which the intruding flow is generated (i.e. by applying the collapse technique or by using flaps) is a crucial factor in determining which type of bulge arises. The observed departure from the solidon behaviour suggests that in the present intrusion experiment the action of relatively small viscous effects is important.

Additional laboratory experiments were carried out to reveal the detailed flow structure in the bulge region. The experiments were performed in the smaller tank (see § 2.1); quantitative flow measurements were made by using the particle tracking system DigImage. Figure 7(*a*, *b*) shows the measured distributions of the stream function ψ and the vorticity ω for an experiment with parameter values $\phi = 6$ and $\theta = 0.46$ (exp. 401, table 1). Although no internal cell structure is observed in the ψ-plot, the ω-distribution (although noisy) suggests an internal four-cell pattern. In particular the outer vortex cells are quite pronounced, while the inner cell pair is weak. It is estimated that the error in the determination of the vorticity values amounts to approximately 15%. The main reason for this limited accuracy is an insufficient

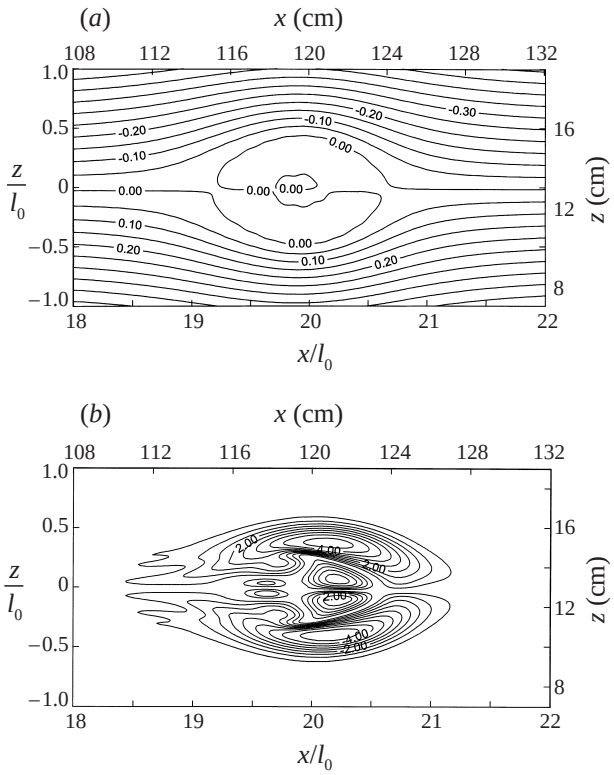

FIGURE 8. Results of numerical simulation of the experiment shown in figure 7: (*a*) streamline pattern in co-moving frame, (*b*) vorticity distribution.

number of tracer particles, which results in a relatively poor representation of the velocity field in the inner region of the bulge. In spite of the noise in the vorticity plot presented in figure 7(*b*), however, the four-cell pattern is clearly recognizable.

Numerical calculations were carried out on a finer grid (300×200), and figure 8 shows some computational results of the bulge structure for exp. 401 at $N_s t = 42.7$: the streamline pattern in the co-moving frame (*a*) and the vorticity distribution (*b*). These plots clearly reveal the existence of a structure of four cells in the advancing bulge. The internal circulation, even though weak, generates inner cells (with weak tails) containing vorticity that is comparable with that in the outer cells. In fact, the two inner 'tail cells' became apparent when the numerical calculations were repeated on a grid that was twice as fine. The existence of the four-cell pattern does not depend on the geometry (circular or square cross-section) of the collapsing fluid volume: the same structure was also found in the computations presented in figure 4(*b*). In fact, a similar four-cell structure inside a large-amplitude solitary bulge advancing through a pycnocline was found in the numerical study of Terez & Knio (1998).

The horizontal velocity u and the vorticity ω along a vertical cross-section through the centre of the bulge as derived from the flow measurements are plotted in figure 9. The characteristic dimple in the $u(z)$ profile at the bulge axis is indicative of the presence of two inner vorticity cells (as can also be concluded from the presence of the relative extrema in the $\omega(z)$ profile near the bulge axis). Although the peaks in the bulge interior are more pronounced in the simulation profiles, the agreement between the experimental and simulation results is obvious; the small deviations are due to the

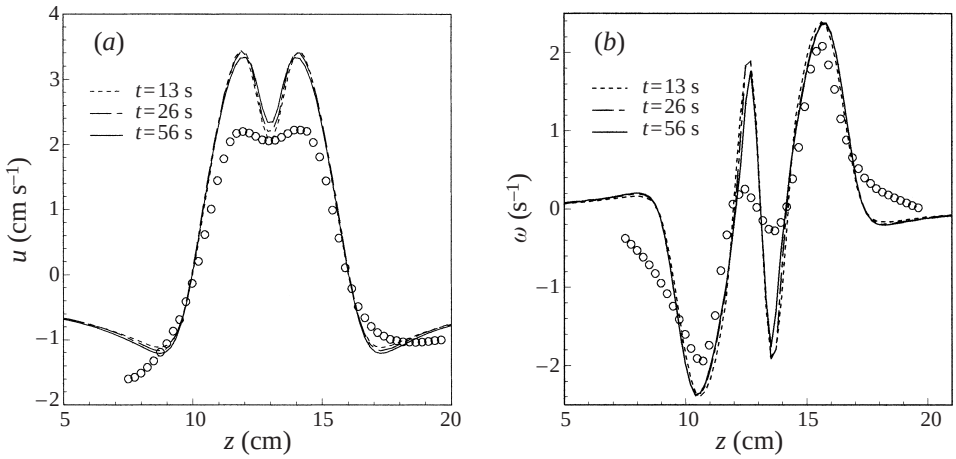

FIGURE 9. Profiles of (*a*) the horizontal velocity u and (*b*) the vorticity ω along a vertical cross-section through the centre of the frontal bulge of figures 7 and 8: ○, experimental results; the curves represent numerical simulation results at $t = 13, 26, 56$ s, respectively.

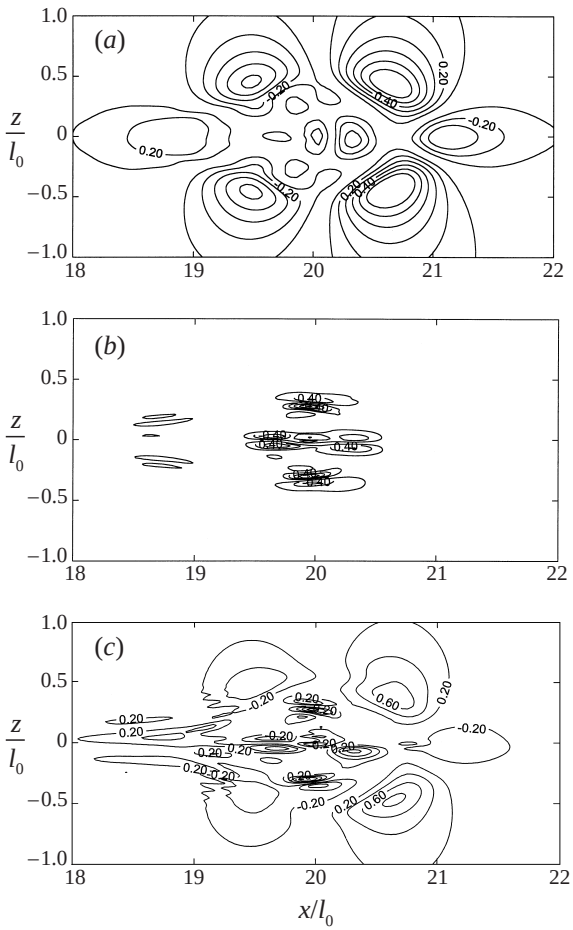

FIGURE 10. Contour plots of the buoyancy (*a*), viscous (*b*) and advection (*c*) terms in the vorticity equation calculated (in the co-moving frame) for the situation shown in figure 8.

Exp.	N (s^{-1})	H (cm)	f (s^{-1})	U_i ($cm\,s^{-1}$)	L_0 (cm)	U_w ($cm\,s^{-1}$)	L_w (cm)
401	0.73	17.0	2.0	1.31	2.93	3.01	59.7
404	0.96	18.3	2.0	1.38	2.56	4.56	66.8
408	1.07	15.5	2.0	1.69	2.42	4.67	—
413	1.25	16.8	2.0	1.50	2.24	5.50	—
415	1.40	15.9	2.0	1.88	2.11	5.50	59.1
417	0.72	18.2	2.0	1.22	2.94	3.49	64.3
419	0.54	14.7	2.0	0.93	3.40	—	—
420	0.50	15.4	2.0	0.84	3.55	2.28	62.7
501	1.03	12.8	2.0	1.50	2.47	3.94	52.4
502	1.04	9.0	2.0	1.42	2.46	3.33	43.3
503	0.90	6.8	2.0	2.23	2.65	2.67	26.5
504	1.08	24.2	2.0	1.56	2.42	5.80	—
505	1.01	17.6	2.0	1.50	2.50	4.57	64.5
601	1.04	16.7	2.5	1.78	2.75	4.97	58.1
602	1.02	17.0	1.6	1.31	2.22	4.50	63.5

TABLE 3. Grid-stirring experiments.

insufficient spatial resolution in the laboratory experiments. As can be seen in figure 9, the profiles of u and ω calculated for different times remain very close, indicating that the four-cell structure is not a transient feature of the flow.

Figure 10 shows contour plots of the buoyancy (*a*), viscous (*b*) and advection (*c*) terms as calculated numerically (in the co-moving frame) for the bulge structure presented in figure 8. The graphs have been plotted on the same scale, to facilitate accurate comparison and hence an analysis of the vorticity balance. It is thus found that the outer cells are associated with baroclinic generation of vorticity: the baroclinic production term and the advection term are the dominating ones in the vorticity equation. In contrast, the numerical calculations revealed that in the inner cells the balance is between the advective and viscous terms. This picture is somewhat different from what is claimed by Terez & Knio (1998), who state that the oppositely signed vorticity in the inner cells is due to oppositely signed baroclinic generation of vorticity.

3.2. *Grid-generated intrusion*

In the second set of intrusion experiments a mixed region was generated by a vertically oscillating, horizontal grid. The dynamics of the intrusion flows in the pycnocline associated with this type of forcing also depends on a large set of parameters, including the depth D of the tank, the pycnocline thickness H, the density difference $\Delta\rho$ across the pycnocline and the oscillating grid characteristics (length L_m, mesh size M, stroke S, frequency f). In the experiments to be discussed here only three parameters were changed, while the others were kept constant. The varied parameters are: the pycnocline thickness H; the buoyancy frequency of the linear density distribution within the pycnocline, defined as $N = (g\Delta\rho/\rho H)^{1/2}$, with $\Delta\rho = \rho_2 - \rho_1$; and the grid oscillation frequency f. These parameters H, N and f were varied systematically, so that three classes of experiments can be distinguished: in each only one parameter was varied, while the other two were kept at their nominal values (experimental parameter values are given in table 3). By careful filling of the tank, a linear density distribution was created within the pycnocline, with a well-

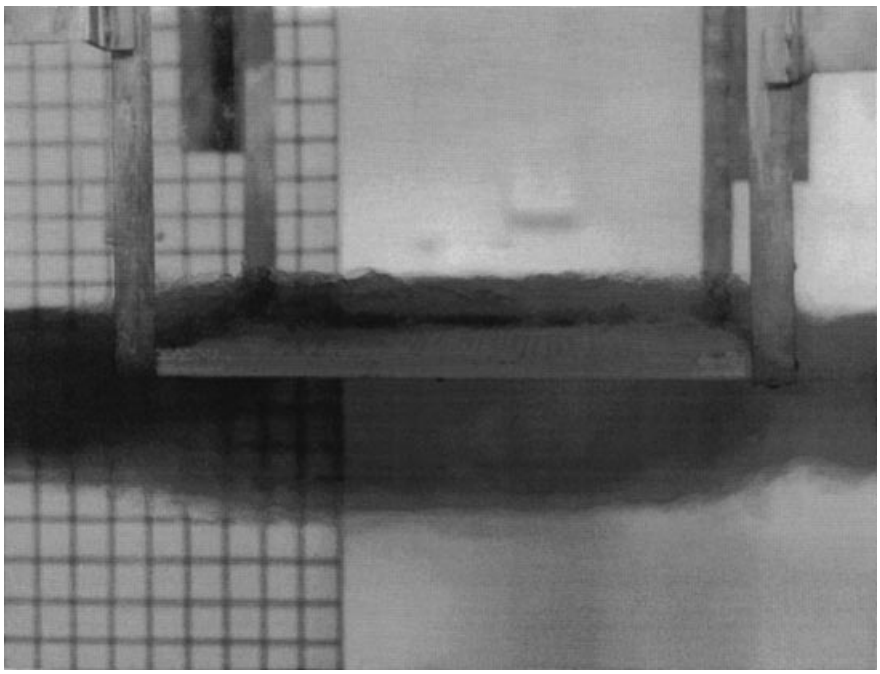

FIGURE 11. Photograph showing the dye-visualized mixed region near the oscillating grid. The four dark vertical bands are metal supporting bars, which are connected to the corners of the grid. The distance between the supports at the front is roughly equal to the length of the grid, i.e. 38 cm.

defined thickness H. With time, however, sharp gradients were removed by diffusion, so that the resulting $\rho(z)$-profiles also resembled the tanh-profile for the case of thin pycnoclines very well, just as in the previous set of experiments (as shown in figure 2).

The grid stirring resulted in a volume of mixed fluid near the grid. This region collapsed under gravity soon after the start of the stirring, which gave rise to an intrusive density current within the pycnocline, directed away from the oscillating grid. The turbulent motion within the intrusion was quickly suppressed by buoyancy forces, so that the intrusive motion at some distance from the grid can be considered as laminar. A photograph of the dye-visualized motion induced by the oscillating grid is shown in figure 11. The flow is visualized by dark dye that was added to the fluid near the grid before the stirring was started. One can clearly observe traces of turbulent entrainment above and below the mixed region. The photograph also shows horizontal, intrusive outflows at either side of the grid, driven by bouyancy forces. A most remarkable feature is the 'necking' of the intrusive current visible on the right-hand side of the grid (this feature is not visible on the other side because the camera was not exactly aligned with the middle of the grid, as can be seen from the four supporting vertical bars). This necking indicates the occurrence of a hydraulic jump, in which the supercritical turbulent outflow shows a transition to a subcritical intrusion flow. Based on qualitative observations of the dyed intrusion from above it was clear that the flow was, with the exception of thin boundary layers at the sidewalls, uniform across the tank. In fact, small deviations from two-dimensionality in the initial, highly-turbulent collapse region were quickly rectified, within a distance of typically 10 cm from the grid. Such two-dimensionality was also noted by Stamp & Jacka (1995).

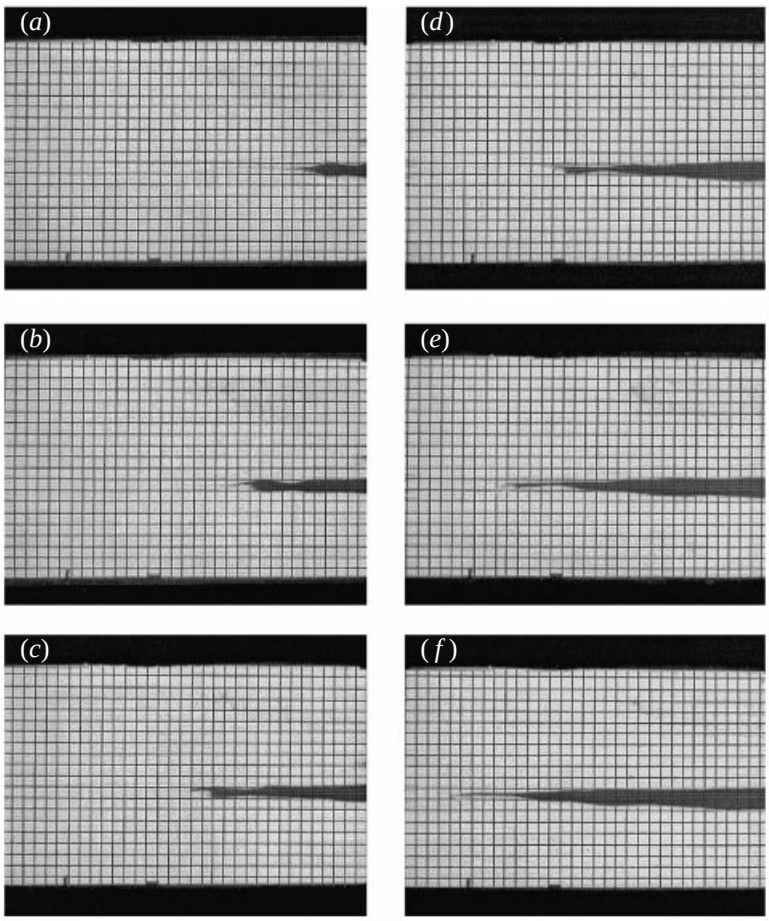

FIGURE 12. Sequence of photographs showing the evolution of the dye-visualized intrusion (now moving to the left) in the oscillating grid experiment 503 for (*a*) $Nt = 856$, (*b*) 910, (*c*) 947, (*d*) 994, (*e*) 1037, (*f*) 1081. Information about the scale of the intrusion is provided by the grid attached to the back wall; the mesh side is 2.54 cm.

The main features of the intrusion can be seen in figure 12, which presents a sequence of side-view photographs of a dye-visualized intrusion experiment. In most cases the intrusion nose was initially rather blunt, but it took on a pointed appearance at distances of typically a few tens of centimetres from the edge of the grid. In the experiment shown in figure 12 the pycnocline was relatively thin (experiment 503, see table 3), i.e. its thickness was comparable to that of the intrusion. In this case the deformation of both the upper and lower sides of the intrusion, similar to what can be seen in figure 3(*a*), is indicative of the dominating presence of a mode-2 component (in the presence of a weaker mode-1 component) in the internal wave field.

By measuring the nose position at regular time intervals it appeared that – at least in the test section – the speed of advance U_i was to good approximation constant in time. The mean values of U_i are given in table 3. The fact that the intrusion speed is constant in time in all experiments is quite remarkable; this suggests that the intrusive flow was in all cases in some quasi-equilibrium state. This observation appears to be in contrast to the experiments of Browand & Hopfinger (1985) and Browand, Guyomar & Yoon (1987) in which intrusions were generated by a vertical grid oscillating in a

linearly stratified fluid. However, our observations are in accordance with those of Maxworthy & Monismith (1988), who performed intrusion experiments in which the mixing was accomplished by a vertically oscillating, horizontal grid at one of the tank ends; in their experiment, however, the grid was located outside the pycnocline, near the free surface.

The intrusive flow is possibly controlled by an inertial–buoyancy balance near the edge of the stirring grid (Manins 1976; Maxworthy & Monismith 1988). In a linearly stratified fluid the condition for inertial control of the intrusion is

$$Fr = U_i/hN \sim 1, \tag{9}$$

with h the intrusion thickness. In a quasi-equilibrium state this thickness h can be related to the Ozmidov scale L_0 (Ozmidov 1965), which is a maximal vertical scale in stratified turbulent flows, here defined as

$$L_0 = \left(\frac{u'^3}{l_t N^3}\right)^{1/2}, \tag{10}$$

with u' the r.m.s. vertical turbulent velocity and l_t the turbulent integral scale. Here N has been taken to be the constant buoyancy frequency in the pycnocline region, the extent of which was greater than the intrusion thickness h (with the exception of experiment 503, as will be discussed below). According to Hopfinger & Toly (1976),

$$u' \sim K z^{-1} \tag{11}$$

$$l_t \sim z, \tag{12}$$

where z is the vertical distance from the grid, and $K = S^{3/2}M^{1/2}f$ is the grid parameter. It is hypothesized that in the equilibrium state $h \sim L_0$. After substitution of (11) and (12) into (10) with $z = h \sim L_0$, one then obtains $L_0 \sim (K/N)^{1/2}$. For the present experiments the calculated values of L_0 are given in table 3. Inertial control of the intrusion according to (9) thus implies

$$U_i \sim L_0 N. \tag{13}$$

Another approach was taken by Maxworthy & Monismith (1988), who derived the following estimate for U_i from a mass balance in the stirring region:

$$U_i \sim h w_e / L_m, \tag{14}$$

where

$$w_e \sim u'/Ri^{3/2} \tag{15}$$

is the entrainment velocity, and

$$Ri = l_t^2 N^2 / u'^2 \tag{16}$$

is the local Richardson number. By combination of these expressions one obtains

$$U_i \sim L_0 N (L_m/L_0)^{1/9}. \tag{17}$$

This relation differs from (13) only by a weak dependence on the ratio of grid length L_m and Ozmidov scale L_0. The measured values of U_i/L_0N are plotted in figure 13 against L_0/L_m (although no error bars have been added, the estimated accuracy of the measured velocity data is better than 10% – as in subsequent data plots). The curve represents the power relation (17), which seems to correspond to the data, although the relation (13) seems to fit equally well. A remarkable exception is experiment

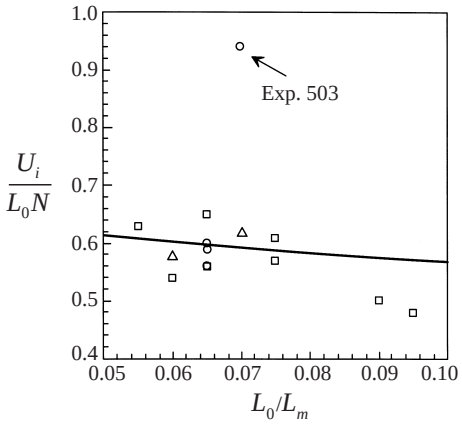

FIGURE 13. The normalized intrusion speed U_i/L_0N as a function of L_0/L_m as measured in experiment series 4 (□), 5 (○) and 6 (△), see table 3. The curve represents the theoretical relation (17).

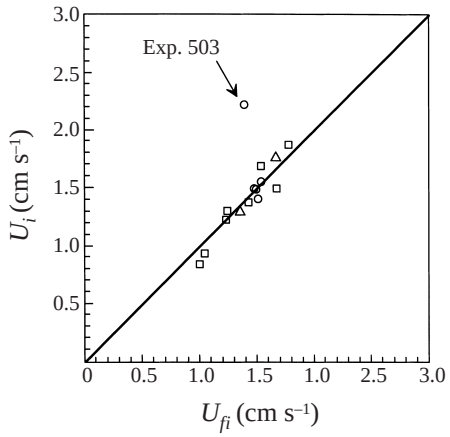

FIGURE 14. Graphical presentation of the measured speed U_i versus the speed U_{fi} according to (18). Symbols have the same meaning as in figure 13.

503 mentioned earlier, in which the intrusion thickness h (= 8.3 cm) exceeds the pycnocline thickness H (= 6.8 cm). In this particular experiment, the intrusive flow is propagating along a thin interface rather than through a uniformly stratified region, and a significantly different behaviour from the other runs is therefore not unexpected.

By substitution of the expressions for K and L_0, the relation (17) can be written in terms of the experimental parameters:

$$U_{fi} = c(S^6 M^2 L_m N^5 f^4)^{1/9}, \tag{18}$$

where c is a proportionality constant. A least-squares fit to the experimental data yields $c = 0.47$, and the result is presented in figure 14: the good agreement with the data supports the hypothesis of the inertially controlled outflow. Again, experiment 503 is the exception, due to the relative thinness of the pycnocline region compared to the intrusion thickness in this run.

In order to explain their experimental data, Maxworthy & Monismith (1988) also considered a viscous–buoyancy balance of the outflow, which yielded $U_i \sim$

$N^2h^4K^{-1}L_m^{-1}$, or

$$U_i \sim L_0 N (L_m/L_0)^{-1/3}. \tag{19}$$

Although this result agrees very well with the experimental data of Maxworthy & Monismith, it shows a significant discrepancy with our observations. The reason for this disagreement lies most likely in the difference in the geometry and the experimental parameter values. The ratio of the inertial and viscous forces is estimated by the parameter $R = h^3(L_m L_0^2)^{-1}$: in the case of Maxworthy and Monismith it took values $R \leqslant 1$, whereas in the present experiments $R \geqslant 1$.

It was observed that the Froude number Fr of the intrusion is approximately constant during the principal stage of the flow evolution, in contrast to the experiments of Browand & Hopfinger (1985), in which Fr decreased with time. The Fr-values did not exceed 0.2, except for the case of exp. 503. The value of the Reynolds number $Re = U_i h/\nu$ was in all cases relatively high (1100–1900), so that the flow is governed by an inertial balance. Theoretically (see Manins 1976; Kao 1976), the Froude number of such intrusions should be $Fr = \frac{1}{2}$. The systematic deviation from this theoretical value is probably due to partial mixing of the fluid by the grid, resulting in horizontally inhomogeneous conditions that lead to diminishing buoyancy forces in the intrusion. Indirect evidence of this partial mixing is obtained from the observation of 'double noses' at the tip of the intrusion as well as from the observed deceleration of the intrusive flow at a distance of typically 2–3 m downstream of the test area. In most runs it was observed that – after having passed the test section – the intrusion slowed down, and finally stopped before reaching the end of the tank, in spite of the continuing stirring by the grid. This behaviour can be explained by the changing structure of the density distribution in the region upstream of the intrusion: because of the finite tank size, the fluid pushed forward by the intrusion results in a vertical displacement of isopycnals in the upstream region. Eventually a stage is reached in which the vertical density gradients upstream and downstream of the intrusion become comparable, thus diminishing the driving buoyancy force, resulting in the arresting of the intrusion. Similar effects were noticed in the experiments by Abramian & Kudin (1983) and Maxworthy & Monismith (1988). At this stage the 'intrusive mode' vanishes, giving way to the 'vortical mode': careful observation of the flow near the tip of the intrusion revealed the occurrence of large pancake-shaped eddies. The motion within these eddies was observed to be purely horizontal. As in other studies on decaying quasi-two-dimensional flows in a rectangular container (van Heijst, Davies & Davis 1990; Flór 1994), the maximum size of the eddies is determined by the smallest length scale of the flow domain, i.e. the width of the tank.

As mentioned before, the collapse of mixed fluid also results in internal waves, which propagate through the pycnocline, ahead of the intrusion. These internal waves have not been visualized, but their occurrence has been measured with the two sets of conductivity probes shown in figure 1. A set of typical 'displacement' signals from the probes is presented in figure 15. A general feature visible in most of the signals is a steep rise for the upper probes and a steep fall for the lower probes, followed by an almost regular wave pattern. The upper and lower displacements are observed to be approximately 180° out of phase, indicating a travelling internal wave of mode 2. Although most probe signals are regular, the signals of probes 2–4 become irregular after a while: these fluctuations indicate remnants of turbulent motions in the passing intrusion.

The average speed U_w of the internal waves in the test section was measured from the time difference in the probe signals of array 1 and 2, and the measured values

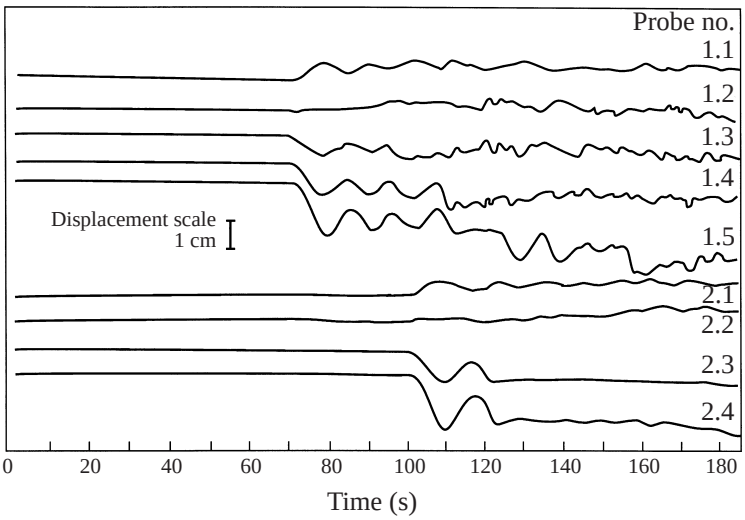

FIGURE 15. Typical probe signals from the stationary probe rakes 1 and 2 in the grid-stirring experiment.

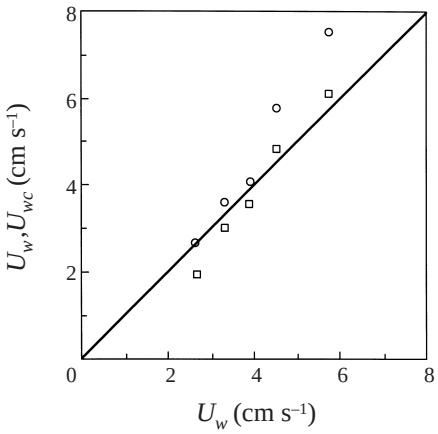

FIGURE 16. Measured values of the internal wave speed U_w in experiment series 5 (see table 3) versus the theoretical estimates (6) and (20), represented by the symbols ○ and □, respectively.

are given in table 3. The characteristics of internal waves of permanent form in a pycnocline located halfway between the tank bottom and the free surface depend on the ratios H/D, H/L_w and $2a/H$, where L_w is the characteristic wavelength and a is the amplitude of the wave displacement. In the present experiments these ratios had values in the following intervals: $0.14 \leqslant H/D \leqslant 0.50$, $0.21 \leqslant H/L_w \leqslant 0.29$ and $0 < 2a/H \leqslant 0.9$. Apparently, effects of both finite depth and nonlinearity may be important in the dynamics of these waves. In figure 16 the measured values of U_w for experiment series 5 (see table 3) are compared with the computed value U_c predicted by (6) according to the weakly nonlinear deep-water Benjamin–Ono theory, and also with the zeroth-order wave velocity

$$U_{wc} = \left\{ \frac{2g\Delta\rho}{\rho_0(2+3\gamma)\alpha} \right\}^{1/2} \tag{20}$$

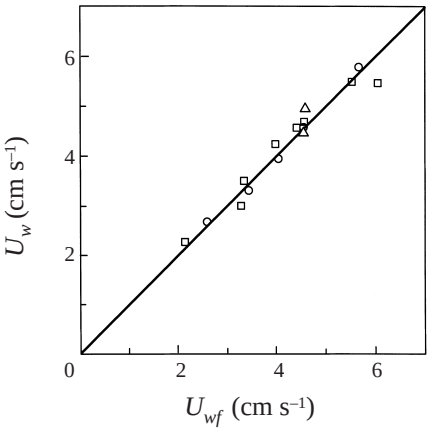

FIGURE 17. Measured values of the internal wave speed U_w versus the empirical relationship (21) for the grid-stirring experiments series 4, 5 and 6. Symbols have the same meaning as in figure 13.

of waves in a layer of finite depth (Kao & Pao 1979), with $\gamma = [\ln(\cosh \frac{1}{2}\alpha D)]^{-1}$. As remarked before, the density profiles in the various runs were approximated quite well by (2). It turns out, however, that the theoretical predictions U_c and U_{wc} do not agree with the measured wave speeds in the full range of the experimental values. As seen in figure 16, the best fit with the Benjamin–Ono theory is obtained for small velocities, i.e. for relatively large pycnocline thickness and short wavelengths. On the other hand, the Kao & Pao result (20) shows a better agreement for $U_w > 4\,\mathrm{cm\,s^{-1}}$. Obviously, the restricting assumptions made for the derivation of these theoretical expressions are not valid in all the cases met here; most likely a numerical solution of the wave problem as carried out by e.g. Kubota, Ko & Dobbs (1978) would yield a better agreement with the experimental data.

Alternatively, we have fitted the wave speed data with the following simple relation (partially suggested by dimensional arguments):

$$U_{wf} = \alpha_1 H N (H/D)^{\beta_1}. \tag{21}$$

The least-squares fit (see figure 17) provides the following values of the constants:

$$\alpha_1 = 0.15 \pm 0.01, \quad \beta_1 = -0.53 \pm 0.05. \tag{22}$$

An estimate of the mean wavelength L_w can be obtained from the probe signals by measuring the time between successive wave crests and multiplying with the mean wave speed U_w for that particular experiment. It was thus found that the wavelength of the internal wave varied between 43 cm and 66 cm (see Table 3). (Note that we have disregarded the value 26 cm measured in the 'exceptional' experiment 503, in which the intrusion was 'bulge-like' rather than wavelike.) The data showed no clear correlation between L_w and N, but a least-squares analysis revealed the following relation between the wavelength and the depths H and D:

$$L_{wf} = \alpha_2 H (H/D)^{\beta_2}, \tag{23}$$

with $\alpha_2 = 2.32 \pm 0.15$ and $\beta_2 = -0.44 \pm 0.06$. Although the experimental results are not plotted here, the scatter in the data was found to be small.

4. Conclusions

In the present study of intrusive flow and internal waves in a pycnocline layer between two homogeneous fluids, a comparison was made between motion generated by short-duration forcing (mixed-region collapse) and intrusive motion arising from long-duration forcing (continuous grid stirring). In particular, the effect of the pycnocline layer depth on the intrusion and the internal wave motion was addressed. Here we briefly summarize the main results.

In the mixed-region collapse experiments it was observed that the intrusion slows down rapidly in the case of a relatively thick pycnocline ($\phi \lesssim 1$), whereas it is approximately constant for at least $Nt \lesssim 50$ in the case of a thin pycnocline ($\phi \gg 1$). Experimental data are presented in figure 5, together with simulation results. On the other hand, in the continuous grid-stirring experiments, in a thick pycnocline the intrusion speed was found to be approximately constant, irrespective of the pycnocline thickness. The measured speeds were compared with a theoretical prediction based on the assumption of inertially controlled outflow from the mixed region; the good agreement (see figure 14) supports the validity of this assumption.

It was observed that intrusive bulges occur in the case of mixed-region collapse in a relatively thin pycnocline; in contrast, in a relatively thick pycnocline the intrusion had a rather sharp nose. The experiments with continuous grid stirring gave no evidence of internal bulges.

From dye-visualization studies, it can be concluded that the intrusion bulge contains fluid that originates from the initial mixed region. Detailed measurements of the flow within the bulge revealed a complicated internal structure consisting of four vortices. The analysis of the vorticity balance (as calculated numerically in the co-moving frame, see figures 8 and 10) revealed that the outer cells are associated with baroclinic generation of vorticity, while the inner cells are characterized by a balance between the advective and the viscous terms in the vorticity equation.

In the oscillating-grid experiments, both intrusive flow and internal wave motion were observed to arise. In all cases considered the internal waves were of the second mode, and their propagation speed was larger than that of the intrusion. As stated before, the intrusion speed is approximately constant and is predicted well by an analytical approximation based on the assumption of an inertial–buoyancy balance in the discharge of the mixed region.

Based on the results of both the mixed-region collapse and the oscillating-grid experiment (as well as prior related studies) it can be stated that almost any pycnocline modulation will generate an intrusive flow as well as a propagating internal wave field. The nature of the internal wave field depends primarily on the amplitude of the disturbance. For small αa the mode-2 internal waves have open streamlines and generally agree with weakly nonlinear theory. For large αa the waves contain, initially at least, recirculation cells that result in a finite mass transport. The speed of the intrusive flow seems to depend on the generating mechanism, being essentially constant in the inertially controlled outflow and steadily increasing in the case of a finite region collapse. These experiments illustrate a range of processes that can exist in highly stratified coastal and estuarine environments and can contribute to local mixing processes that can, in turn, affect the water column structure and thus the bio-chemical distributions.

The authors gratefully acknowledge the constructive comments of the anonymous referees on an earlier version of the paper. V. S. M. is indebted to Alexey Kulik and Irina Avdeyeva for their part in the Kiev experiments and calculations.

REFERENCES

Abramian, T. O. & Kudin, A. M. 1983 Laboratory study of the interaction of mixed fluid patches at their spreading in a stratified medium. *Izv. Akad. Nauk. SSSR, Phys. Atmos. Ocean* **18**, 888–892.

Amen, R. & Maxworthy, T. 1980 The gravitational collapse of a mixed region into a linearly stratified fluid. *J. Fluid Mech.* **96**, 65–80.

Benjamin, T. B. 1967 Internal waves of permanent form in fluids of great depth. *J. Fluid Mech.* **29**, 559–592.

Brandt, A. & Heijst, G. J. F. van 1990 Laboratory experiments on intrusive flow in a linearly stratified pycnocline. In *Stratified Flows* (ed. E. J. List & G. H. Jirka), pp. 666–674. ASCE.

Brandt, A., Sarabun, C. C., Dubbel, D. C. & Vogt, C. J. 1986*a* Estuarine internal wave stability and breaking. Presented at *AGU/ASLO Conference, New Orleans.* (Abstract *EOS. Trans. Am. Geophys. Union* **66** (51), 1269 (1995).)

Brandt, A., Sarabun, C. C., Seliger, H. H. & Tyler, M. A. 1986*b* The effects of the broad spectrum of physical activity on the biological processes in the Chesapeake Bay. In *Marine Interfaces Hydrodynamics* (ed. J. C. J. Nihoul), pp. 361–384. Elsevier.

Browand, F. K., Guyomar, D. & Yoon, S.-C. 1987 The behaviour of a turbulent front in a stratified fluid: experiments with an oscillating grid. *J. Geophys. Res.* **95**, 5329–5341.

Browand, F. K. & Hopfinger, E. J. 1985 The inhibition of vertical turbulent scale by stable stratification. In *Turbulence and Diffusion in Stable Environments*, (ed. J. C. R. Hunt), pp. 15–27. Clarendon, Oxford.

Chernyshenko, S. 1993 Stratified Sadovskii flow in a channel. *J. Fluid Mech.* **250**, 423–432.

Dalziel, S. B. 1993 Rayleigh-Taylor instability experiments with image analysis. *Dyn. Atmos. Oceans* **20**, 127–154.

Davis, R. E. & Acrivos, A. 1967 Solitary internal waves in deep water. *J. Fluid Mech.* **29**, 593–607.

De Silva, I. P. D. & Fernando, H. J. S. 1998 Experiments on collapsing turbulent regions in stratified fluids. *J. Fluid Mech.* **358**, 29–60.

Fernando, H. J. S. 1991 Turbulent mixing in stratified fluids. *Ann. Rev. Fluid Mech.* **23**, 455–493.

Flór, J. B. 1994 Coherent vortex structures in stratified fluids. PhD thesis, Eindhoven University of Technology, The Netherlands.

Flór, J. B., Fernando, H. J. S. & Heijst, G. J. F. van 1994 The evolution of an isolated turbulent region in a two-layer fluid. *Phys. Fluids* **6**, 287–296.

Fonseka, S. V., Fernando, H. J. S. & Heijst, G. J. F. van 1998 Evolution of an isolated turbulent region in a stratified fluid. *J. Geophys. Res.* C **103**, 24857–24868.

Garrett, C., MacCready, P. & Rhines, P. 1993 Boundary mixing and arrested Ekman layers. *Ann. Rev. Fluid Mech.* **25**, 291–323.

Guschin, V. A. 1981 The method of splitting for the solution of problems of dynamics of inhomogeneous viscous incompressible fluids. *Zh. Vychisl. Mat. i Mat. Fiz.* **21**, 1003–1017.

Heijst, G. J. F. van, Davies, P. A. & Davis, R. G. 1990 Spin-up in a rectangular container. *Phys. Fluids* A **2**, 150–159.

Hopfinger, E. J. 1987 Turbulence in stratified fluids: A review. *J. Geophys. Res.* **92**, 5287–5303.

Hopfinger, E. J. & Toly, J.-A. 1976 Spatially decaying turbulence and its relation to mixing across density interfaces. *J. Fluid Mech.* **78**, 155–175.

Hurdis, D. A. & Pao, H.-P. 1975 Experimental observation of internal solitary waves in a stratified fluid. *Phys. Fluids* **18**, 385–386.

Ivey, G. N., & Corcos, G. M. 1982 Boundary mixing in a stratified fluid. *J. Fluid Mech.* **121**, 1–26.

Kamachi, M. & Honji, H. 1982 Steady flow patterns of internal solitary bulges in a stratified fluid. *Phys. Fluids* **25**, 1119–1120.

Kao, T. W. 1976 Principal stage of wake collapse in a stratified fluid: Two-dimensional theory. *Phys. Fluids* **19**, 1071–1074.

Kao, T. W. & Pao, H.-P. 1980 Wake collapse in the thermocline and internal solitary waves. *J. Fluid Mech.* **97**, 116–127.

Kozlov, V. F. & Makarov, V. G. 1990 On a class of stationary gravity currents with a density jump. *Izv. Akad. Nauk. SSSR, Phys. Atmos. Ocean* **26**, 395–402.

Kubota, T., Ko, D. R. S. & Dobbs, L. D. 1978 Weakly-nonlinear, long internal gravity waves in stratified fluids of finite depth. *J. Hydronautics* **12**, 157–165.

Levtsov, V. I. & Chashechkin, Yu. D. 1980 Highly sensitive contact-type electrical conduc-

tivity probe and a device for its static calibration. *Proc. 1st All-Union Conf. on Metrology of Hydrophysical Measurements*, p. 46. Standart, Moscow.

MADERICH, V. S. & KULIK, A. I. 1992 Laboratory experiments on the collapse of an intrusion in a layered medium. *Izv. Akad. Nauk. SSSR, Phys. Atmos. Ocean* **28**, 1197–1204.

MADERICH, V. S., NIKISHOV, V. I. & STETSENKO, A. G. 1988 *Dynamics of Internal Turbulent Mixing in a Stratified Medium.* Naukova Dumka, Kiev.

MANINS, P. C. 1976 Intrusion into a stratified fluid. *J. Fluid Mech.* **74**, 547–560.

MAXWORTHY, T. 1980 On the formation of nonlinear internal waves from the gravitational collapse of mixed regions in two and three dimensions. *J. Fluid Mech.* **96**, 47–64.

MAXWORTHY, T. & MONISMITH, S. G. 1988 Differential mixing in a stratified fluid. *J. Fluid Mech.* **189**, 571–598.

OZMIDOV, R.V. 1965 On the turbulent exchange in a stably stratified ocean. *Izv. Acad. Sci. USSR, Atmos. Ocean. Phys.* (Engl. Transl.) **1**, 493–497.

PADMANABHAN, H., AMES, W. F., KENNEDY, J. F. & HUNG, T. K. 1970 A numerical investigation of wake deformation in density stratified fluids. *J. Engng Maths* **4**, 229–241.

PHILLIPS, O. M., SHYU, J. A. & SALMUN, H. 1986 An experiment on boundary mixing: mean transport and circulation rates. *J. Fluid Mech.* **173**, 473–499.

SALMUN, H. & PHILLIPS, O. M. 1992 An experiment on boundary mixing. Part 2. The slope dependence at small angles. *J. Fluid Mech.* **240**, 355–377.

SIMPSON, J. E. 1997 *Gravity Currents in the Environment and the Laboratory*, 2nd Edn. Cambridge University Press.

STAMP, A. P. & JACKA, M. 1995 Deep-water internal solitary waves. *J. Fluid Mech.* **305**, 347–371.

TEREZ, D. E. & KNIO, O. M. 1998 Numerical simulations of large-amplitude internal solitary waves. *J. Fluid Mech.* **362**, 53–82.

THORPE, S. A. 1982 On the layers produced by rapidly oscillating a vertical grid in a uniformly stratified fluid. *J. Fluid Mech.* **124**, 391–409.

WU, J. 1969 Mixed region collapse with internal wave generation in a density stratified medium. *J. Fluid Mech.* **35**, 531–544.